



Light-tuned switching of charge transfer channel for simultaneously boosted photoactivity and stability

Yang-Shan Xie^{a,b}, Lan Yuan^{a,b}, Nan Zhang^{a,b}, Yi-Jun Xu^{a,b,*}

^a State Key Laboratory of Photocatalysis on Energy and Environment, College of Chemistry, Fuzhou University, Fuzhou, 350116, PR China

^b College of Chemistry, New Campus, Fuzhou University, Fuzhou, 350116, PR China

ARTICLE INFO

Keywords:

Nanorod heterostructure arrays
Z-scheme heterojunction
Type-II heterojunction
Anti-photocorrosion

ABSTRACT

The design and construction of semiconductor-based photocatalysts with high activity and stability toward redox reactions is an imperative requirement for practical photocatalytic applications. Here, we report that tuning light irradiation from visible light to UV–vis light can simultaneously improve the photocatalytic activity and stability of ternary ZnO–CdS–MoS₂ (ZCM) heterostructure catalyst for H₂ evolution, which is enabled by switching the interfacial charge transfer channel from the conventional type-II charge transfer pathway to the direct Z-scheme pathway. The Z-scheme system boosts more efficient charge carrier separation and consumption of holes and electrons for respective redox processes, thereby resulting in more distinct activity enhancement and particularly photocorrosion inhibition than the type-II system over the ZCM photocatalyst.

1. Introduction

The development of new renewable energy technologies has stirred mounting interests in harvesting solar energy. Photocatalysis, with the ability to utilize solar energy for producing solar fuels and alleviating environmental pollution, has been regarded as a promising photoconversion technology [1–3]. Yet so far, the photoconversion efficiency is still far from practical application owing to the undesirable charge carriers recombination and inferior solar light utilization efficiency of semiconductor-based photocatalyst systems [4,5]. Because single-component semiconductor photocatalyst cannot simultaneously satisfy the requirements of efficient charge carriers separation and broad spectrum absorption, controllable design of heterojunctions has been developed to be an effective approach to build composite photocatalytic system toward efficiently harvesting light and steering the spatial separation/transfer of electron-hole pairs, thereby enhancing the photocatalytic redox performance for target reactions [6–15].

To date, various heterojunction photocatalysts, such as conventional band alignment (type-I, type-II and type-III) [16–18], Z-scheme system [19–22], p–n junction [23–25], surface heterojunction [26] and semiconductor-graphene heterostructures [27,28], have been demonstrated to show enhanced photocatalytic activity by suppressing the recombination of photoinduced electrons and holes. Although these studies have put on a critical consideration of the interface (for

example, interfacial trapping site, lattice and surface electron or hole trapping sites) and recombination of charge carriers in multiple material components, the underlying origin of the long-term photostability of semiconductors, especially for the easily photocorroded semiconductors (such as CdS and ZnO), remains elusive. In addition, considering that the stability of photocatalysts is closely linked to the separation and transfer pathway of photogenerated charge carriers, it is reasonable to infer that the selective manipulation of charge flow channels could be feasible for alleviating the photocorrosion of semiconductor-based photocatalysts and improving their photoactivity simultaneously.

Herein, we have reported the significant effect of switching charge transfer channel from the conventional type-II to direct Z-scheme charge transfer channels, which is realized by tuning light irradiation from visible light to UV–vis light, on the photocatalytic activity and photostability of ternary ZnO–CdS–MoS₂ (ZCM) core-shell heterostructure catalyst. The ZCM photocatalyst consists of a ZnO nanorod core and CdS–MoS₂ shell, where the CdS shell is directly grown on a ZnO nanorod core arrays and MoS₂ nanoparticles are further covered on the CdS shell matrix. The results show that as compared to the type-II band alignment, the Z-scheme band alignment enables more efficient charge separation and transfer, timely consumption of holes and electrons, and thus more significant improvement in both photocatalytic activity for H₂ evolution and anti-photocorrosion capability.

* Corresponding author at: State Key Laboratory of Photocatalysis on Energy and Environment, College of Chemistry, Fuzhou University, Fuzhou, 350116, PR China.

E-mail address: yjxu@fzu.edu.cn (Y.-J. Xu).

<https://doi.org/10.1016/j.apcatb.2018.07.006>

Received 23 April 2018; Received in revised form 29 June 2018; Accepted 2 July 2018

Available online 03 July 2018

0926-3373/ © 2018 Elsevier B.V. All rights reserved.

2. Experimental section

2.1. Materials

All chemicals were analytical grade and obtained from commercial suppliers and used without further purification. Zinc nitrate hexahydrate ($\text{Zn}(\text{NO}_3)_2 \cdot 6\text{H}_2\text{O}$), ammonium acetate ($\text{CH}_3\text{COONH}_4$, NH_4Ac), hexamethylene tetramine ($\text{C}_6\text{H}_{12}\text{N}_4$, HMT), cadmium chloride ($\text{CdCl}_2 \cdot 2.5\text{H}_2\text{O}$), sublimed sulfur (S_8), methanol (CH_3OH), ammonium tetrathiomolybdate ($(\text{NH}_4)_2\text{MoS}_4$), absolute ethanol ($\text{C}_2\text{H}_5\text{OH}$) were obtained from Sinopharm Chemical Reagent Co., Ltd. (Shanghai, China). Fluorine-doped tin oxide (FTO)-coated glass substrates (resistance $< 14 \text{ ohm/sq}$, transmittance $> 90\%$) were purchased from Wuhan Jing-Solar Energy Technology Co., Ltd. Deionized water used in the synthesis was from local sources.

2.2. Catalyst preparation

2.2.1. Synthesis of ZnO nanorod arrays

Prior to the deposition of ZnO nanorod arrays, the FTO coated glass substrates were cleaned with detergent under sonication for 90 min, followed by washing with deionized water. Then, ZnO nanorods were deposited onto the pre-cleaned FTO-coated glass substrates using an electrochemical approach in a three electrodes system. The FTO substrate, platinum (Pt) foil and Ag/AgCl electrode were used as the working, counter and reference electrodes, respectively. The ZnO seed layer was initially deposited over an FTO substrate in a 50 mL solution containing 0.02 M $\text{Zn}(\text{NO}_3)_2 \cdot 6\text{H}_2\text{O}$, 0.01 M NH_4Ac and 0.01 M HMT with a potential of -1.3 V vs. Ag/AgCl for 10 s at 90°C . In the second step, a constant potential of -1.0 V vs. Ag/AgCl was applied for 2000 s. The resulting sample was washed with deionized water three times, dried with a stream of N_2 and then annealed at 350°C in air. Then the obtained ZnO nanorod arrays were labeled as Z NRAs.

2.2.2. Synthesis of ZnO-CdS nanorod arrays

The ZnO nanorod arrays coated FTO glass was immersed in 50 mL of methanol containing 20 mg $\text{CdCl}_2 \cdot 2.5\text{H}_2\text{O}$ and 5 mg S_8 and deaerated by N_2 bubbling for 0.5 h in the dark. Then, the stable suspension was irradiated with UV-vis light by a 300 W Xe arc lamp (PLS-SXE 300, Beijing Perfectlight) for 1 h under continuous N_2 bubbling at the flow rate of 80 mL min^{-1} . The resulting sample was washed with deionized water three times, and dried with a stream of N_2 . The as-prepared films were denoted as ZC NRAs.

2.2.3. Synthesis of ZnO-CdS-MoS₂ nanorod arrays

The ZnO-CdS nanorod arrays coated FTO glass was immersed in a 50 mL mixture of ethanol (10 mL) and deionized water (40 mL) that contained a certain amount of $(\text{NH}_4)_2\text{MoS}_4$ and then irradiated with visible light ($\lambda > 420 \text{ nm}$) for 1 h. N_2 was continuously bubbled through the sample solution before and during the irradiation to remove oxygen completely. The as-prepared sample was washed with deionized water three times and dried with a stream of N_2 . The molar ratio for Mo/Cd in the initial photocatalyst precursors is 0.05, 0.1, 0.3, 0.5 and 1 wt%, respectively. Then the obtained ZnO-CdS-MoS₂ core-shell nanorod arrays were labeled as ZCM-0.05, ZCM-0.1, ZCM-0.3, ZCM-0.5 and ZCM-1, respectively.

2.2.4. Synthesis of ZnO-MoS₂ nanorod arrays

The preparation of ZnO-MoS₂ core-shell nanorod arrays was the same as that of ZnO-CdS-MoS₂ nanorod arrays except using the ZnO nanorod arrays and UV-vis light to replace the ZnO-CdS counterpart and visible light. Besides, the sample was denoted as ZM NRAs.

2.3. Characterizations

The morphology of the samples was determined by field emission

scanning electron microscopy (FESEM) on a Hitachi New Generation cold field emission SEM SU-8000 spectrophotometer. Transmission electron microscopy (TEM) and high-resolution transmission electron microscopy (HRTEM) were analyzed using a JEOL model JEM 2010 EX instrument at an acceleration voltage of 200 kV. The X-ray diffraction (XRD) patterns of the samples were measured on a Bruker D8 Advance X-ray diffractometer with $\text{Cu K}\alpha$ radiation in the 2θ ranging from 10 to 80° at a scan rate of $0.02^\circ \text{ s}^{-1}$. The optical properties of the samples were characterized by UV-vis diffuse reflectance spectroscopy (DRS) using UV-vis spectrophotometer (Cary 500, Varian Co.) in which BaSO_4 was employed as a reference in the range of 250–750 nm. X-ray photoelectron spectroscopy (XPS) was performed on a Thermo Scientific ESCA Lab 250 spectrometer, which was made of a monochromatic Al $\text{K}\alpha$ as the X-ray source, a hemispherical analyzer, and a sample stage with multiaxial adjustability to obtain the surface composition of the samples. All of the binding energies were calibrated by the $\text{Cl } 1\text{s}$ peak at 284.6 eV. The photoluminescence spectra (PL) for samples were analyzed on an Edinburgh Analytical Instrument F900 spectrophotometer with an excitation wavelength of 320 nm and 450 nm. To ensure the comparability of the PL spectra, the experimental parameters, including the excitation wavelength, slit width, and the amount of the samples, were identical. In particular, the generation of hydroxyl radicals in solution was detected by the PL technique with terephthalic acid (PL-TA) as a probe molecule. The sample films ($25 \text{ mm} \times 10 \text{ mm}$) were vertically dipped into a $5 \times 10^{-3} \text{ M}$ TA aqueous solution containing a concentration of 0.01 M NaOH and irradiated with UV-vis light ($800 \text{ nm} > \lambda > 300 \text{ nm}$) for 1 h by a 300 W Xe arc lamp (PLS-SXE 300, Beijing Perfectlight). The UV-vis light irradiation was continuous and sampling was performed every 10 min for analysis. The photoelectrochemical analysis was composed of conventional three-electrode, a quartz cell containing 30 mL Na_2SO_4 (0.5 M) aqueous solution. A platinum plate ($10 \text{ mm} \times 10 \text{ mm}$) was used as the counter electrode, Ag/AgCl as reference electrode and the synthesized catalysts as the working electrodes. The sample films ($25 \text{ mm} \times 10 \text{ mm}$) were vertically dipped into electrolyte and irradiated with visible light ($\lambda > 420 \text{ nm}$) or UV-vis light ($800 \text{ nm} > \lambda > 300 \text{ nm}$) by a 300 W Xe arc lamp (PLS-SXE 300, Beijing Perfectlight). The electrochemical impedance spectroscopy (EIS) experiments were conducted on an electrochemical workstation (Autolab, PGSTAT204) in the electrolyte of 0.5 M KCl aqueous solution containing 0.01 M $\text{K}_3[\text{Fe}(\text{CN})_6]/\text{K}_4[\text{Fe}(\text{CN})_6]$ (1:1) under open-circuit potential conditions and irradiated with visible light ($\lambda > 420 \text{ nm}$) or UV-vis light ($800 \text{ nm} > \lambda > 300 \text{ nm}$) by a 300 W Xe arc lamp (PLS-SXE 300, Beijing Perfectlight). Incident photon-to-current conversion efficiency (IPCE) was collected by PEC-S20 (Pecell Technology Co. Ltd.) without bias potential. The incident light was provided by AM 1.5 solar simulator and the light intensity was calibrated with a standard solar cell for amorphous silicon solar cell produced by Japan Quality Assurance Organization.

2.4. Photocatalytic activity

The photocatalytic reaction was performed in a quartz reactor. For each reaction, the sample films ($25 \text{ mm} \times 10 \text{ mm}$) were vertically dipped into 8 mL deionized water containing 0.35 M Na_2S and 0.25 M Na_2SO_3 as the sacrificial agents. The reaction solution was evacuated by a mechanical pump several times to remove air completely prior to irradiation. The photocatalytic system was irradiated with visible light ($\lambda > 420 \text{ nm}$) or UV-vis light ($800 \text{ nm} > \lambda > 300 \text{ nm}$) by a 300 W Xe arc lamp (PLS-SXE 300, Beijing Perfectlight) with energy output of 0.75 W/cm^2 measured by a Thor labs PM100 optical power and energy meter which was placed at a distance of approximate 10 cm or 8 cm with the reactor. The photocatalytic reaction was typically performed for 2 h, and 1 mL of reactive gas was taken from the reactor with a syringe for analysis using a gas chromatograph (GC 2014C, 5 A molecular sieve column, TCD, Ar carrier). The recycling test of catalytic H_2 evolution over the used catalyst was done as follows. Typically, after

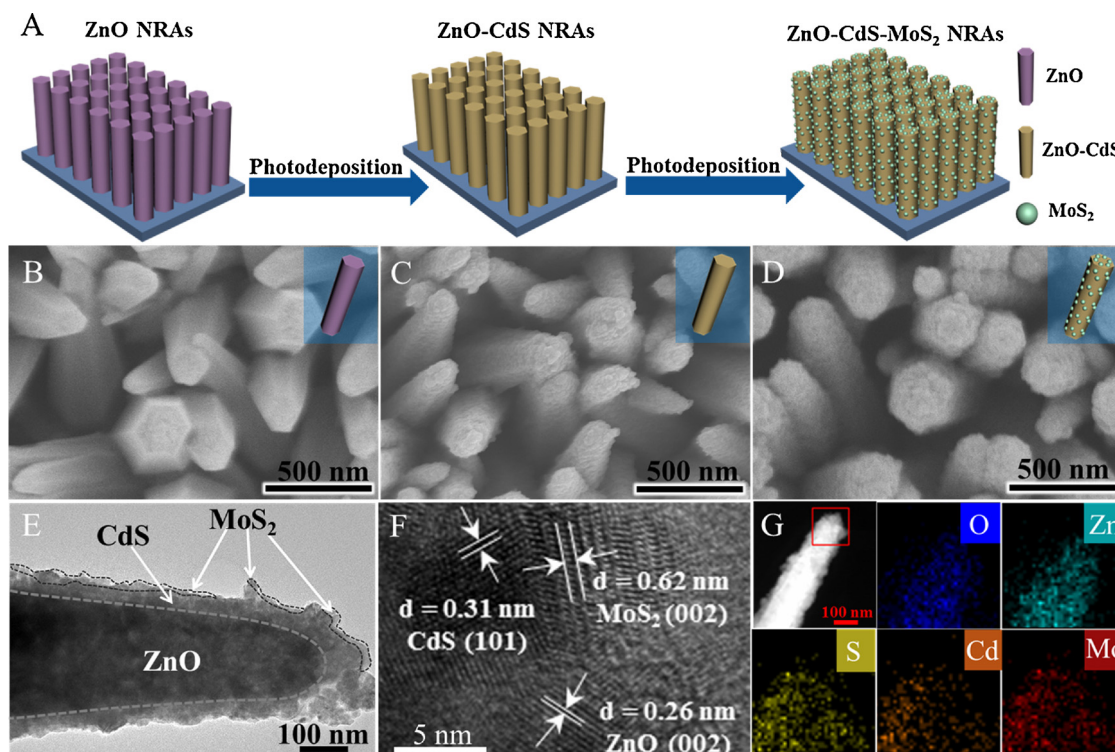


Fig. 1. Schematic illustration of the synthesis of the ZnO-CdS-MoS₂(ZCM) core-shell NRAs (A); top view FESEM images of ZnO (Z) NRAs (B), ZnO-CdS (ZC) core-shell NRAs (C) and ZCM NRAs (D); the insets of B, C and D show the corresponding schematic models; TEM image (E), HRTEM image (F) and elemental mapping results (G) of ZCMNRAs.

the reaction of the first run under light irradiation for 2 h, the photocatalytic system was thoroughly degassed again, without the separation of photocatalysts or the supplement of sacrificial agents. Subsequently, the thoroughly degassed system was irradiated again with visible light ($\lambda > 420$ nm) or UV-vis light ($800\text{ nm} > \lambda > 300$ nm) by a 300 W Xe arc lamp (PLS-SXE 300C, Beijing Perfectlight). Analogously, the following runs of photocatalytic recycling tests were performed. The concentration of the leached Cd^{2+} in solution was quantified by an inductively coupled plasma emission spectroscopy instrument (ICP, PerkinElmer Optima 8000).

3. Results and discussion

The overall fabrication procedure for ternary ZnO-CdS-MoS₂ core-shell nanorod arrays (ZCM NRAs) heterostructure is schematically depicted in Fig. 1A. ZnO nanorod arrays (Z NRAs) have been firstly synthesized over the surface of a fluorine doped tin oxide (FTO) glass substrate using the electrochemical deposition method. The morphology of the Z NRAs has been observed by field-emission scanning electron microscopy (FESEM). As displayed in Fig. 1B and S1A, the Z NRAs framework consists of a compact array of vertically aligned and highly ordered ZnO nanorods with a smooth surface. Meanwhile, cross-sectional FESEM image shows a fairly consistent length of Z NRAs, which is about $2.8\text{ }\mu\text{m}$ (Fig. S1B). Using the as-prepared Z NRAs as fundamental building blocks, binary ZnO-CdS nanorod arrays (ZC NRAs) and ternary ZCM NRAs are fabricated through photodeposition method. As is clearly seen, the surface of ZC NRAs (Fig. 1C and S1C) and ZCM NRAs (Fig. 1D and S1D) heterostructures has been remarkably altered to become rather rough, which can be ascribed predominantly to the deposition of uniformly dispersed CdS and MoS₂. Meanwhile, cross-sectional FESEM image in Fig. S1E verifies ordered structure of ZCM NRAs substrate with a length of ca. $2.8\text{ }\mu\text{m}$, corroborating the well-maintained vertically aligned Z NRAs backbones after the CdS and MoS₂ photodeposition process. To further investigate the microscopic

particularly interface structure of the as-prepared ZCM NRAs, transmission electron microscopy (TEM) measurements have been performed. Fig. 1E reveals that the ZnO nanorod is fully covered by CdS and MoS₂ nanoparticles to form core-shell architecture, which suggests an intimate contact among the MoS₂ cocatalyst, CdS and ZnO NRAs. Fig. 1F shows the different lattice fringes with d-spacing of 0.26 nm, 0.31 nm and 0.62 nm, which are assigned to ZnO (002), CdS (101) and MoS₂ (002), respectively. All elements can be detected in ZCM NRAs from energy-dispersive X-ray spectroscopy (EDX) spectrum, as disclosed in Fig. S1F. Moreover, the corresponding elemental mapping further certifies the elemental distribution of ZCM NRAs (Fig. 1G). The elements of O, Zn, S, Cd and Mo are evenly distributed within the entire ZCM NRAs heterostructure, in which S, Cd and Mo elements are covered on O and Zn elements. These results evidence the successful formation of vertically aligned core-shell ZCM NRAs on FTO substrate.

The crystallographic structures of FTO glass and as-prepared samples have been analyzed by X-ray diffraction (XRD). As revealed in Fig. 2A, besides the diffraction peaks from FTO substrate, all the diffraction peaks of pure Z NRAs are ascribed to the wurtzite hexagonal structure of ZnO (JCPDS No. 36-1451) and the predominant (002) peak implies the growth along the [0001] c-axis for the ZnO nanorods [29,30]. The diffraction peaks at 2θ values of 31.8° , 34.4° , 36.3° , 47.5° , 56.6° , 62.9° , 68.0° and 72.6° can be assigned to (100), (002), (101), (102), (110), (103), (112) and (004) facets of wurtzite ZnO, respectively. Notably, an additional weak diffraction peak located at 28.2° appears among the samples of ZC NRAs and ZCM NRAs, which is attributed to (101) facet of hexagonal CdS (JCPDS No.41-1049) (Fig. 2B), in agreement with the corresponding HRTEM result. Meanwhile, no typical diffraction peaks of MoS₂ have been detected, which can be ascribed to its limited amount and well dispersion [31]. Furthermore, the optical properties of different samples have been determined by UV-vis diffuse reflectance spectra (DRS). As shown in Fig. 2C, it is apparent to see that Z NRAs show a significant absorption edge at wavelength around 400 nm, correlating with the wide bandgap of ZnO [32]. ZC NRAs

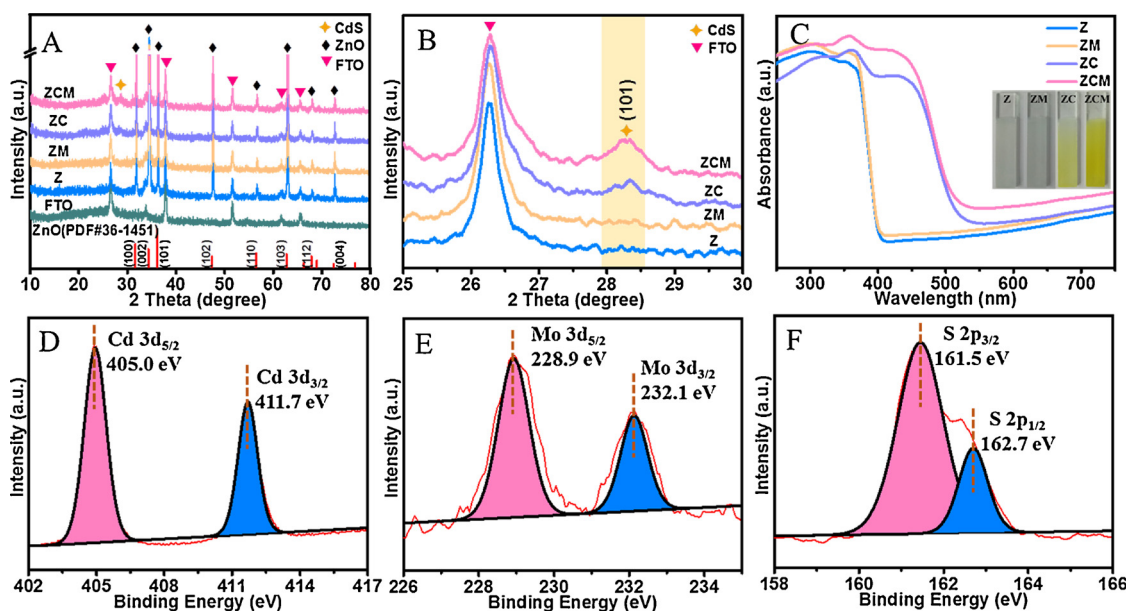


Fig. 2. XRD patterns (A,B) and UV-vis diffuse reflectance spectra (C) of Z NRs, ZM NRs, ZC NRs and ZCM NRs; the inset of (C) shows the corresponding photographs of different samples; high-resolution XPS spectra of Cd 3d (D), Mo 3d (E) and S 2p (F) of ZCM NRs.

exhibit a strong and broad absorption in the visible light region of 400–500 nm due to the absorption of CdS semiconductor [33], which is in line with color change of the samples (the inset of Fig. 2C). After hybridization of MoS₂ cocatalyst with ZC NRs, the absorption of ZCM NRs in visible light region from 500 to 750 nm is enhanced with the increase of MoS₂ content (Fig. S2) [34,35]. According to the Tauc plots of $(\alpha h\nu)^2$ versus photo energy ($h\nu$) [36], the calculated bandgap energy for blank ZNRs and ZMNRs samples are determined to be 3.13 and 3.10 eV, respectively (Fig. S3). The bandgap of ZC NRs and ZCM NRs are estimated from the absorption edges of CdS to be 2.39 and 2.36 eV, respectively. These values indicate that the obtained ZnO NRs after deposition of CdS and MoS₂ exhibit strong absorption in both UV and visible light regions.

To further probe the composition and chemical valence states of ZCM NRs heterostructure, the X-ray photoelectron spectroscopy (XPS) analysis has been performed. Survey spectrum of ZCM NRs confirms the coexistence of Zn, O, Cd, S and Mo elements in the ternary composite (Fig. S4A), which is in agreement with the EDX results. As shown in Fig. S4B, two characteristic peaks located at binding energy of about 1021.6 and 1044.6 eV are ascribed to Zn 2p_{3/2} and Zn 2p_{1/2}, respectively, which agree well with Zn element in ZnO [37–39]. In addition, in Fig. S4C, the binding energy of O 1s peak at 530.5 eV is usually attributed to the O²⁻ in wurtzite ZnO [36]. The peaks at 405.0 and 411.7 eV in Cd3d spectrum are characteristic of the Cd²⁺ in CdS (Fig. 2D) [39–41]. Fig. 2E presents two strong peaks located at 228.9 and 232.1 eV, which are in good agreement with Mo 3d_{5/2} and Mo 3d_{3/2} of Mo⁴⁺, respectively [41]. The binding energy of S 2p_{3/2} at 161.5 and S 2p_{1/2} at 162.7 eV in Fig. 2F is assigned to S²⁻, which are ascribed to the hybrid chemical bond species of Cd-S and Mo-S [42]. The XPS analysis results further confirm the successful assembly of ZnO, CdS and MoS₂ to form the ternary core-shell heterostructure.

Photocatalytic H₂ evolution activities of various samples have been firstly evaluated under visible light ($\lambda > 420$ nm) irradiation with the addition of Na₂S and Na₂SO₃ as the sacrificial agents. The photoactivity results over Z NRs, ZM NRs, ZC NRs and ZCM NRs are depicted in Fig. 3A. It can be observed that the pure Z NRs and ZM NRs show negligible and low activities, respectively. When the Z NRs are coupled with visible-light-driven CdS photocatalyst, ZC NRs give rise to a remarkably photoactivity improvement toward H₂ evolution. As the subsequent introduction of MoS₂ component into the matrix of ZC

NRs, the H₂ production over ZCM NRs composite exceeds that over the Z NRs, ZM NRs and ZC NRs counterparts. Among the ZCM NRs samples with different contents of MoS₂, the one with 0.3 wt % MoS₂ loading displays the highest photoactivity of H₂ evolution (Fig. S5).

To gain an insight into the origin of significantly enhanced photocatalytic H₂ evolution activity of ZCM NRs as compared to other counterparts, the photoelectrochemical characterizations and photoluminescence (PL) analyses have been carried out to comparatively investigate the charge carriers transfer and separation processes. Fig. 3B shows transient photocurrent responses of the samples under intermittent visible light irradiation. The bare Z NRs show negligible photocurrent response while the photocurrent density of binary ZC NRs is enhanced after the introduction of visible light responsive CdS. The subsequent assembly of MoS₂ to form ternary ZCM NRs is able to remarkably further elevate the photocurrent density. Both the binary ZM NRs and ZC NRs composites show much lower photocurrent density than ternary ZCM NRs, suggesting that the combined synergy of CdS and MoS₂ can effectively promote the separation of electron-hole pairs photogenerated in such a ternary core-shell architecture. Moreover, the intensity of PL peak at 395 nm over Z NRs diminishes with the addition of MoS₂ or CdS and further quenches drastically by the synergistic contributions of MoS₂ and CdS, strongly demonstrating the more effectively inhibited recombination of charge carriers photo-generated from ZnO nanorods by loading CdS and MoS₂ (Fig. S6). In addition, these results are further confirmed by lifetime of photoelectrons under visible light irradiation that has been measured by open circuit photovoltage (V_{oc}) decay (OCP) technique [43]. The calculated electron life time as a function of V_{oc} is shown in Fig. S7, from which it is clearly seen that ZCM NRs exhibit the prolonged electron lifetime in comparison with single and binary counterparts. The electrochemical impedance spectroscopy (EIS) has also been conducted to explore the charge transfer progress at the contact interface between sample and electrolyte (Fig. 3C). The Nyquist diagram of ZCM NRs shows the smallest semicircle at high frequency among these four samples, revealing that a smaller resistance and a more efficient charge transfer between ZCM NRs composite and electrolyte solution are obtained than those over ZC NRs, ZM NRs and bare Z NRs. To estimate the relationship between light absorption and the photocurrent density of the samples, incident photon to current conversion efficiency (IPCE)

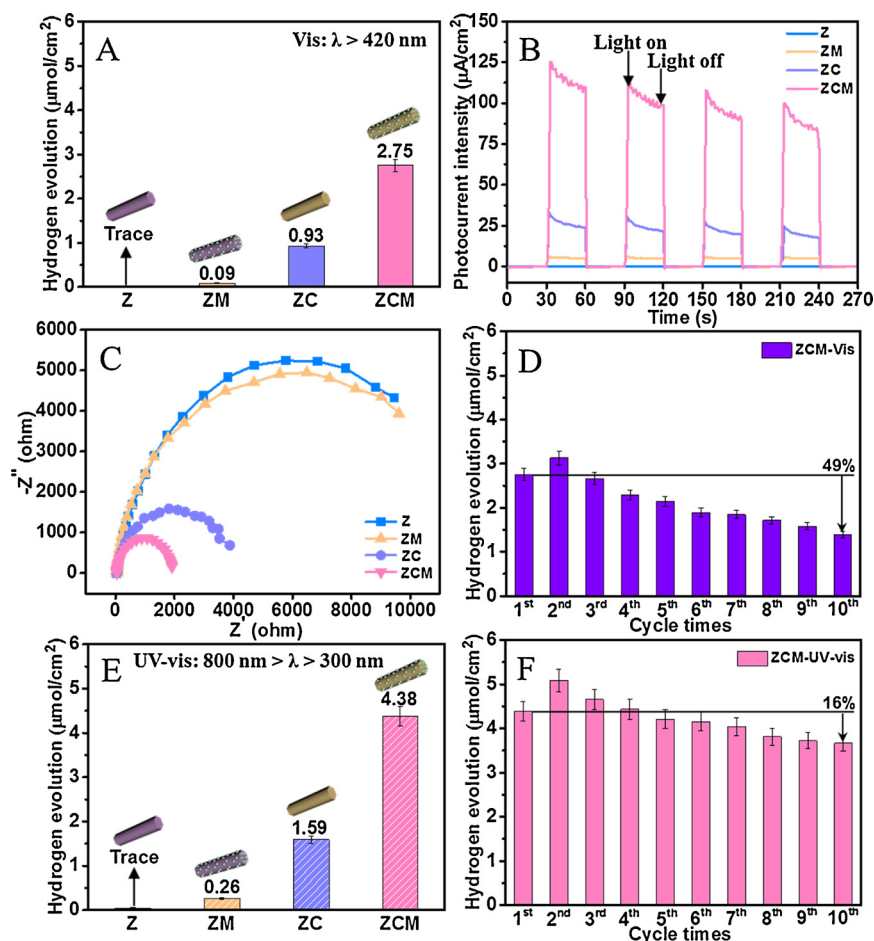


Fig. 3. Photocatalytic H_2 evolution of Z NRAs, ZM NRAs, ZC NRAs and ZCM NRAs under visible light irradiation for 2 h (A); transient photocurrent responses (B) and electrochemical impedance spectroscopy (EIS) Nyquist plots (C) of Z NRAs, ZM NRAs, ZC NRAs and ZCM NRAs under visible light irradiation; cycling test of photocatalytic H_2 evolution for ZCM NRAs under visible light irradiation for 20 h (D); photocatalytic H_2 evolution of Z NRAs, ZM NRAs, ZC NRAs and ZCM NRAs under UV-vis light irradiation for 2 h (E); cycling test of photocatalytic H_2 evolution for ZCM NRAs under UV-vis light irradiation for 20 h (F).

measurement has been performed. It can be seen from Fig. S8 that the pristine Z NRAs only exhibit substantial IPCE in the UV region, while IPCE responses of the ZC NRAs and ZCM NRAs in the visible regions are significantly enhanced as compared to that of the Z NRAs, in accordance with the improved visible light absorption of ZCM NRAs. However, the recycling experiment in Fig. 3D shows that ZCM NRAs under visible light irradiation (denoted as ZCM-Vis in the following discussions) demonstrates a poor stability with an obvious deactivation activity (49%) after ten successive cycles, inferring that the catalyst should be seriously photocorroded. The higher H_2 generation activity in the second cycle than that in the first cycle should be ascribed to the existence of an induced period at an early stage of irradiation [44,45].

For comparison, when we switch the visible light to UV-vis light irradiation, which possesses equivalent light intensity (0.75 W/cm^2) to the visible light, interesting phenomenon happens. As reflected by Fig. 3E, ZCM NRAs under UV-vis light irradiation (denoted as ZCM-UV-vis in the following discussions) exhibit approximately 2 times enhancement of the H_2 evolution activity after 2 h irradiation as compared with that of ZCM-Vis. To eliminate the influence of the light density on the photocatalytic activity, the wavelength-dependent apparent quantum yield (AQY) for H_2 evolution has been investigated on the ZCM NRAs heterostructure. As elucidated in Fig. S9A, the H_2 evolution activities of ZCM NRAs show a closely coincident relationship with its optical absorption. Besides, the AQY value at 420 nm is estimated to be 0.8% (Fig. S9B), which is comparable with recently reported values of semiconductors for photocatalytic water splitting [22,46]. Notably, the H_2 evolution activity of ZCM-UV-vis remains

relatively stable in the ten reaction cycles for 20 h (Fig. 3F). In addition, as shown in Fig. S10, the binary ZC NRAs show a similar improved photocatalytic activity and stability by tuning light irradiation from visible light to UV-vis light, implying that the different charge transfer modes between ZnO and CdS caused by the rational light switching from visible to UV-vis might be responsible for the enhanced photocatalytic performance and stability. The addition of MoS_2 to act as the cocatalyst for further promoting the charge separation to achieve more stable and efficient photocatalytic H_2 evolution in ZCM NRAs than ZC NRAs. To understand the observed enhancement of photoactivity, photoelectrochemical analyses of ZCM-UV-vis have also been performed. As shown in Fig. S11, under UV-vis light irradiation, an analogous charge separation efficiency trend of different samples follows the orders of ZCM NRAs > ZC NRAs > ZM NRAs > Z NRAs, which is in line with the transient photocurrent, EIS and OCP test results under identical visible light irradiation. To further determine the significantly different H_2 evolution activity under such two light irradiation conditions, the transient photocurrent and EIS results over the two optimal ZCM-UV-vis and ZCM-Vis samples have been further compared. As depicted in Fig. 4A, the photocurrent density of ZCM-UV-vis heterostructure is almost 2.5 times as large as that of ZCM-Vis, suggesting that more efficient charge separation has been realized for ZCM-UV-vis composite than ZCM-Vis. In addition, as evidenced by the Nyquist plots displayed in Fig. 4B, the ZCM-UV-vis sample exhibits a distinctly depressed semicircle at high frequency in comparison with the ZCM-Vis, indicating the more efficient interfacial charge mobility in the ZCM-UV-vis heterostructure catalyst. The above results together consolidate

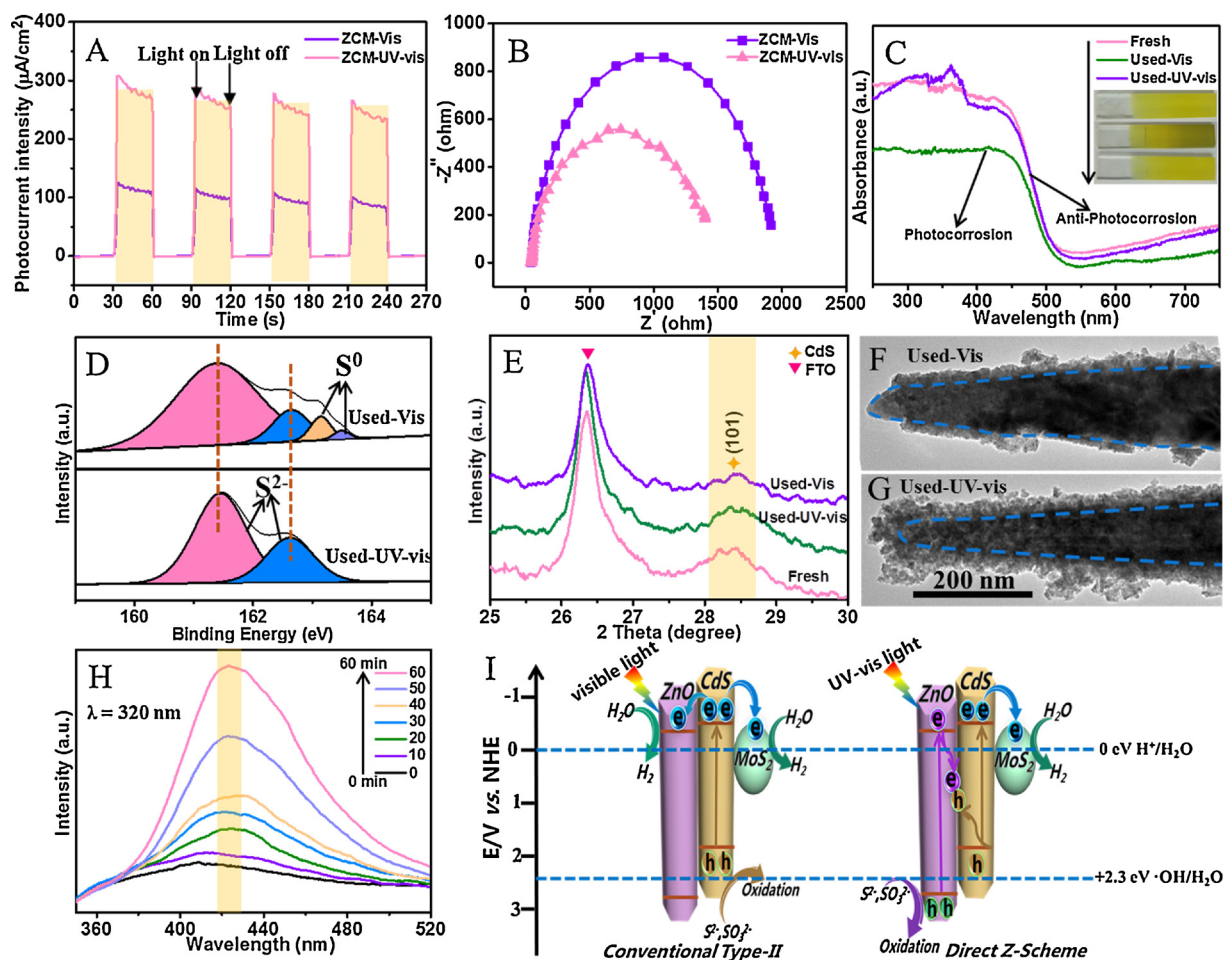


Fig. 4. Comparison of transient photocurrent responses (A) and electrochemical impedance spectroscopy (EIS) Nyquist plots (B) of ZCM NRAs under visible light irradiation and UV-vis light irradiation; UV-vis diffuse reflectance spectra (C), XPS spectra (D) and XRD patterns (E) of fresh and used ZCM NRAs; the inset of C shows the corresponding photographs of samples; TEM images of ZCM NRAs after cycling test under visible light irradiation (F) and UV-vis light irradiation (G); fluorescence spectra (H) of ZCM NRAs in a terephthalic acid solution irradiated by UV-vis light at different irradiation times (excitation at 320 nm) for 1 h; schematic illustration of the proposed mechanism for the photocatalytic hydrogen evolution over the ZCM NRAs heterostructure: switching charge transfer from conventional type II to direct Z-scheme by tuning light irradiation from visible light to UV-vis light (I).

that the enhanced H₂ generation over ZCM-UV-vis should be ascribed to the superior charge transfer channel in ZCM-UV-vis as compared to ZCM-Vis.

To reveal the underlying reason for the enhanced photostability of ZCM-UV-vis as compared to ZCM-Vis, the relative optical response, phase structure and morphology of ZCM-Vis and ZCM-UV-vis samples before and after ten successive recycling tests have been comparatively analyzed. Fig. 4C elucidates the optical properties maintenance in recycled ZCM-UV-vis, implying its improved anti-photocorrosion capability. In contrast, an apparent change of optical-absorption ability has been observed in ZCM-Vis after the recycling photocatalytic reactions, which is ascribed to the formation of S⁰ via the oxidation of surface lattice S²⁻ by the photogenerated holes in ZCM-Vis, as proved by the corresponding XPS spectra of S 2p (Fig. 4D) and the changed color of used ZCM-Vis (the inset of Fig. 4C). Meanwhile, the enhanced anti-photocorrosion performance of ZCM-UV-vis can be further defined by the XPS signal of Cd 3d. As shown in Fig. S12, the CdS composition is almost retained in used ZCM-UV-vis after repeating photocatalytic tests, while the CdS in used ZCM-Vis has been greatly photocorroded as supported by the significantly decreased Cd content. The results from inductively coupled plasma detection (ICP) analysis have also evidenced that there is detectable Cd²⁺ leaching in the reaction solution (0.0434 mg/L) after continuous visible light irradiation of ZCM-Vis (Table S1) aqueous dispersion for 20 h. Furthermore, XRD profile

(Fig. 4E), TEM (Fig. 4F) and SEM images (Fig. S13A) of ZCM-Vis before and after ten cycles photoactivity test collectively certify that the crystalline phase and surface microstructure of the materials are obviously damaged. In sharp contrast, as shown in Fig. 4G and Fig. S13B, no apparently detectable change of morphology over ZCM-UV-vis is observed, indicating improved anti-photocorrosion ability of ZCM-UV-vis. With a well maintained core-shell structure of used ZCM-UV-vis, the 16% fading of photocatalytic H₂ generation activity over ZCM-UV-vis after ten cycles should be attributed to the consumption of the sacrificial agents, rather than the decay of ZCM-UV-vis [37,39]. After refreshing the sacrificial solution, the photocatalytic performances of ZCM-UV-vis are again recoiled to the initial stage (Fig. S14). Therefore, it is reasonable to conclude that the more efficient charge transfer over ZCM-UV-vis results in both enhanced photocorrosion inhibition and higher activity for H₂ evolution.

To further decipher the photocatalytic mechanism for the simultaneously improved photocatalytic activity and stability of ZCM-UV-vis, the PL technique with terephthalic acid (TA) as probe molecules has been used to detect hydroxyl radicals ($\cdot\text{OH}$) over ZCM NRAs [47,48]. As shown in Fig. 4H, the PL intensity at about 426 nm increases gradually with prolonged irradiation time, which indicates the gradual production of $\cdot\text{OH}$ radicals under UV-vis light irradiation. As the edge of valence band (VB) of CdS (1.7 V vs. NHE) is more negative than the potential of $\cdot\text{OH}/\text{H}_2\text{O}$ (2.3 V vs. NHE), the oxidation of H₂O by the

holes in CdS to hydroxyl radicals ($\cdot\text{OH}$) is not thermodynamically feasible (Fig. S15) [48,49]. If ZnO and CdS form a conventional type-II heterostructure, the photogenerated holes are likely transferred from the VB of ZnO to the VB of CdS, thereby exhibiting a negligible or weak PL signal from $\cdot\text{OH}$ radicals, which is inconsistent with the hydroxyl radical experiments. These results demonstrate that the photocatalytic mechanism of ZCM NRAs under UV–vis light irradiation is not in accordance with the conventional type-II charge separation process. Therefore, it can be inferred that a direct Z-scheme photocatalytic system is realized in such ternary ZCM NRAs heterostructure under UV–vis light irradiation, which possesses stronger oxidation ability toward the generation of $\cdot\text{OH}$ [47,50].

On the basis of the above analyses and results, the photocatalytic mechanism for H_2 evolution of ZCM NRAs is proposed, as illustrated in Fig. 4I. Under visible light illumination, energetic electrons and holes are generated from the photoexcitation of CdS in ZCM NRAs, whereas ZnO is not bandgap excited. The electrons localized from the conduction band (CB) of CdS transfer to the CB of ZnO and the deposited MoS_2 following the type-II band alignment to drive the photocatalytic H_2 production processes, while the holes stored in the VB of CdS are trapped by sacrificial agents. As a result, the photogenerated charge recombination can be decreased, leading to an enhanced photoactivity compared with single/binary components. But the remaining holes in the VB of CdS are not timely consumed and then inevitably induce the oxidation of surface lattice S^{2-} ions to form S^0 phase, which results in a low stability of type-II ZCM NRAs. By tuning light irradiation from visible light to UV–vis light, electron-hole pairs are generated in both ZnO and CdS. The electrons in the CB of ZnO are transferred to the VB of CdS and then combine with the holes in CdS, which favorably follow the Z-scheme charge transfer pathway. In this case, the holes with a higher oxidation potential in the VB of ZnO can be efficiently consumed by sacrificial agents. The MoS_2 on the CdS acting as cocatalysts can further capture and transfer the excited electrons in the CB of CdS with higher reduction ability to react with H^+ in solution to form H_2 , which thus result in an efficient spatial separation of photoinduced charge carriers and optimized redox ability. Accordingly, the Z-scheme charge transfer pathway contributes to higher charge carriers separation efficiency, particularly higher reducing capacity of electrons and more timely consumption of holes, than conventional type-II ZCM NRAs heterostructure, thereby leading to an enhancement in both photocatalytic activity and anti-photocorrosion capability for H_2 evolution.

4. Conclusion

In summary, we have unveiled that tuning light irradiation from visible light to UV–vis light can switch the interface heterojunction charge transfer routes over ternary ZnO–CdS– MoS_2 (ZCM) core-shell composites from conventional type-II to direct Z-scheme pathway. Compared with type II charge transfer pathway, the resultant Z-scheme ZCM NRAs photocatalysts show much higher photocatalytic H_2 generation activity and improved anti-photocorrosion ability because Z-scheme charge transfer pathway enables more efficient charge carriers separation and timely consumption of holes. Such charge transfer channel switching strategy presents a paradigm for the rational design of semiconductor-based composite system for manipulating the directional flow of charge carriers to simultaneously meet enhanced activity and stability toward photocatalytic solar energy conversion.

Acknowledgements

The support from the National Natural Science Foundation of China (U1463204, 21173045 and 20903023), the Award Program for Minjiang Scholar Professorship, the Natural Science Foundation of Fujian Province for Distinguished Young Investigator Rolling Grant (2017J07002), the Independent Research Project of State Key Laboratory of Photocatalysis on Energy and Environment (No.

2014A05), the first Program of Fujian Province for Top Creative Young Talents, and the Program for Returned High-Level Overseas Chinese Scholars of Fujian province is kindly acknowledged.

Appendix A. Supplementary data

Supplementary material related to this article can be found, in the online version, at doi:<https://doi.org/10.1016/j.apcatb.2018.07.006>.

References

- [1] S. Bai, J. Jiang, Q. Zhang, Y. Xiong, *Chem. Soc. Rev.* 44 (2015) 2893–2939.
- [2] J. Low, C. Jiang, B. Cheng, S. Wageh, A.A. Al-Ghamdi, J. Yu, *Small Methods* 1 (2017) 1700080.
- [3] A.B. Djurisic, Y.H. Leung, A.M. Ching Ng, *Mater. Horiz.* 1 (2014) 400–410.
- [4] S. Linic, P. Christopher, D.B. Ingram, *Nat. Mater.* 10 (2011) 911–921.
- [5] P. Yang, J.-M. Tarascon, *Nat. Mater.* 11 (2012) 560–563.
- [6] X. Wang, G. Liu, L. Wang, Z.-G. Chen, G.Q. Lu, H.-M. Cheng, *Adv. Energy Mater.* 2 (2012) 42–46.
- [7] B. Qiu, Q. Zhu, M. Du, L. Fan, M. Xing, J. Zhang, *Angew. Chem.* 129 (2017) 2728–2732.
- [8] K. Li, M. Han, R. Chen, S.-L. Li, S.-L. Xie, C. Mao, X. Bu, X.-L. Cao, L.-Z. Dong, P. Feng, Y.-Q. Lan, *Adv. Mater.* 28 (2016) 8906–8911.
- [9] C. Han, N. Zhang, Y.-J. Xu, *Nano Today* 11 (2016) 351–372.
- [10] W. Jiang, X. Zong, L. An, S. Hua, X. Miao, S. Luan, Y. Wen, F.F. Tao, Z. Sun, *ACS Catal.* 8 (2018) 2209–2217.
- [11] S.J.A. Moniz, S.A. Shevlin, D.J. Martin, Z.-X. Guo, J. Tang, *Energy Environ. Sci.* 8 (2015) 731–759.
- [12] Y.-P. Yuan, L.-W. Ruan, J. Barber, S.C. Joachim Loo, C. Xue, *Energy Environ. Sci.* 7 (2014) 3934–3951.
- [13] L. Huang, X. Hu, S. Yuan, H. Li, T. Yan, L. Shi, D. Zhang, *Appl. Catal. B* 203 (2017) 778–788.
- [14] Y. Liu, J. Xu, H. Li, S. Cai, H. Hu, C. Fang, L. Shi, D. Zhang, *J. Mater. Chem. A* 3 (2015) 11543–11553.
- [15] L. Liu, L. Ding, Y. Liu, W. An, S. Lin, Y. Liang, W. Cui, *Appl. Catal. B* 201 (2017) 92–104.
- [16] L. Huang, X. Wang, J. Yang, G. Liu, J. Han, C. Li, *J. Phys. Chem. C* 117 (2013) 11584–11591.
- [17] D.O. Scanlon, C.W. Dunnill, J. Buckeridge, S.A. Shevlin, A.J. Logsdail, S.M. Woodley, C.R.A. Catlow, M.J. Powell, R.G. Palgrave, I.P. Parkin, G.W. Watson, T.W. Keal, P. Sherwood, A. Walsh, A.A. Sokol, *Nat. Mater.* 12 (2013) 798.
- [18] M. Xie, X. Fu, L. Jing, P. Luan, Y. Feng, H. Fu, *Adv. Energy Mater.* 4 (2014) 1300995.
- [19] L. Yuan, B. Weng, J.C. Colmenares, Y. Sun, Y.J. Xu, *Small* 13 (2017) 1702253.
- [20] P. Li, Y. Zhou, H. Li, Q. Xu, X. Meng, X. Wang, M. Xiao, Z. Zou, *Chem. Commun.* 51 (2015) 800–803.
- [21] H. Tada, T. Mitsui, T. Kiyonaga, T. Akita, K. Tanaka, *Nat. Mater.* 5 (2006) 782–786.
- [22] Z. Zhang, J. Huang, Y. Fang, M. Zhang, K. Liu, B. Dong, *Adv. Mater.* 29 (2017) 1606688.
- [23] K. Zhang, W. Kim, M. Ma, X. Shi, J.H. Park, *J. Mater. Chem. A* 3 (2015) 4803–4810.
- [24] J. Zhang, S.Z. Qiao, L. Qi, J. Yu, *Phys. Chem. Chem. Phys.* 15 (2013) 12088–12094.
- [25] M. Wang, L. Sun, Z. Lin, J. Cai, K. Xie, C. Lin, *Energy Environ. Sci.* 6 (2013) 1211–1220.
- [26] J. Yu, J. Low, W. Xiao, P. Zhou, M. Jaroniec, *J. Am. Chem. Soc.* 136 (2014) 8839–8842.
- [27] Q. Li, B. Guo, J. Yu, J. Ran, B. Zhang, H. Yan, J.R. Gong, *J. Am. Chem. Soc.* 133 (2011) 10878–10884.
- [28] C. Han, Z. Chen, N. Zhang, J.C. Colmenares, Y.-J. Xu, *Adv. Funct. Mater.* 25 (2015) 221–229.
- [29] Z. Yin, X. Wang, F. Sun, X. Tong, C. Zhu, Q. Lv, D. Ye, S. Wang, W. Luo, Y. Huang, *Sci. Rep.* 7 (2017) 12206.
- [30] X. Wang, H. Zhu, Y. Xu, H. Wang, Y. Tao, S. Hark, X. Xiao, Q. Li, *ACS Nano* 4 (2010) 3302–3308.
- [31] B. Han, S. Liu, N. Zhang, Y.-J. Xu, Z.-R. Tang, *Appl. Catal. B* 202 (2017) 298–304.
- [32] C.X. Guo, J. Xie, H. Yang, C.M. Li, *Adv. Sci.* 2 (2015) 1500135.
- [33] N. Zhang, S. Xie, B. Weng, Y.-J. Xu, *J. Mater. Chem. A* 4 (2016) 18804–18814.
- [34] K. Zhang, S. Qian, W. Kim, J.K. Kim, X. Sheng, J.Y. Lee, J.H. Park, *Nano Energy* 34 (2017) 481–490.
- [35] F. Ma, Y. Wu, Y. Shao, Y. Zhong, J. Lv, X. Hao, *Nano Energy* 27 (2016) 466–474.
- [36] Y. Feng, G. Wang, J. Liao, W. Li, C. Chen, M. Li, Z. Li, *Sci. Rep.* 7 (2017) 11622.
- [37] S. Mukhopadhyay, I. Mondal, U. Pal, P.S. Devi, *Phys. Chem. Chem. Phys.* 17 (2015) 20407–20415.
- [38] X. Zou, P.-P. Wang, C. Li, J. Zhao, D. Wang, T. Asefa, G.-D. Li, *J. Mater. Chem. A* 2 (2014) 4682–4689.
- [39] G. Yang, W. Yan, Q. Zhang, S. Shen, S. Ding, *Nanoscale* 5 (2013) 12432–12439.
- [40] S. Ding, X. Yin, X. Lü, Y. Wang, F. Huang, D. Wan, *ACS Appl. Mater. Interfaces* 4 (2012) 306–311.
- [41] M.-Q. Yang, C. Han, Y.-J. Xu, *J. Phys. Chem. C* 119 (2015) 27234–27246.
- [42] P.-Y. Kuang, Y.-Z. Su, K. Xiao, Z.-Q. Liu, N. Li, H.-J. Wang, J. Zhang, *ACS Appl. Mater. Interfaces* 7 (2015) 16387–16394.
- [43] B.H. Meekins, P.V. Kamat, *ACS Nano* 3 (2009) 3437–3446.
- [44] Z.-J. Li, X.-B. Li, J.-J. Wang, S. Yu, C.-B. Li, C.-H. Tung, L.-Z. Wu, *Energy Environ.*

- Sci. 6 (2013) 465–469.
- [45] T.-H. Yu, W.-Y. Cheng, K.-J. Chao, S.-Y. Lu, *Nanoscale* 5 (2013) 7356–7360.
- [46] L. Jiang, L. Wang, G. Xu, L. Gu, Y. Yuan, *Sustain. Energy Fuels* 2 (2018) 430–435.
- [47] D. Ma, J.-W. Shi, Y. Zou, Z. Fan, X. Ji, C. Niu, *ACS Appl. Mater. Interfaces* 9 (2017) 25377–25386.
- [48] J. Jin, J. Yu, D. Guo, C. Cui, W. Ho, *Small* 11 (2015) 5262–5271.
- [49] X. Jia, M. Tahir, L. Pan, Z.-F. Huang, X. Zhang, L. Wang, J.-J. Zou, *Appl. Catal. B* 198 (2016) 154–161.
- [50] X. Wang, G. Liu, Z.-G. Chen, F. Li, L. Wang, G.Q. Lu, H.-M. Cheng, *Chem. Commun.* 0 (2009) 3452–3454.